Nanoparticle size distribution estimation by a full-pattern powder diffraction analysis

A. Cervellino*
Laboratory for Neutron Scattering, PSI Villigen and ETH Zurich, , CH-5232 Villigen PSI, Switzerland

C. Giannini,† A. Guagliardi, and M. Ladisa
Consiglio Nazionale delle Ricerche, Istituto di Cristallografia (CNR-IC), Via Amendola 122/O, I-70126 Bari, Italy
(Received 25 February 2005; published 5 July 2005)

The increasing scientific and technological interest in nanoparticles has raised the need for fast, efficient, and precise characterization techniques. Powder diffraction is a very efficient experimental method, as it is straightforward and nondestructive. However, its use for extracting information regarding very small particles brings some common crystallographic approximations to and beyond their limits of validity. Powder pattern diffraction calculation methods are critically discussed, with special focus on spherical particles with log-normal distributions, with the target of determining size distribution parameters. A 20-nm CeO_2 sample is analyzed as an example.

DOI: 10.1103/PhysRevB.72.035412 PACS number(s): 61.10.Nz, 81.07.Bc, 61.46.+w

I. INTRODUCTION

We are assisting at a booming expansion of nanoparticle research and technology. Synthesis methods especially make fast progresses.[1] Analysis methods, however, are not up to speed. A fundamental simple task such as determining and controlling the size distribution of nanoparticles (NPs) is currently a complex experimental work, involving electron microscopy and combined techniques. In this work we want to highlight the possibilities offered in this issue by the much less complex technique of powder diffraction.

Powder diffraction is a widespread technique with a great potential to meet the increasing demands of microstructural material characterization. The methods of powder diffraction data analysis have reached maturity for micrometer-sized polycrystalline materials. However, when the particle size falls much below 100 nm, specifically tuned methods of analysis are needed to extract meaningful information from powder diffraction patterns. In fact, nanoparticles present unique analytical challenges. In the most complex cases, noncrystallographic structures[2–11] may occur. Surface-related deformation fields[12–14] are another challenge. In these extreme cases, the classical crystallographic formalism becomes quite useless. The Debye scattering function[15] (that is, the direct evaluation of the NP structure factor from the interatomic distances) is the only choice in those cases. We are currently developing[10,16] methods to increase the efficiency of such calculations and make them a practical tool.

Even for crystalline NPs, however, the small size plays a decisive role. Bragg peaks may be so much broadened that they cannot be simply separated and many approximations, commonly accepted for micrometer-size domains, fail. As we will show, also models specifically corrected for NPs may fail for ultrasmall NPs (say below 5 nm diameter, as it is better specified).[17–19] Again for these ultrasmall sizes the Debye scattering function is the only choice for obtaining precise results, while the smaller number of atoms makes it extremely practical.

The plan of the paper is the following. In Sec. II we discuss the shape-based method for calculating NP powder patterns in relation to the surface structure and to its limits of validity at small sizes. Application to full-pattern fit on a test case (20-nm CeO_2) is shown in Sec. III.[20] Summary and conclusions are given in Sec. IV.

II. POWDER PATTERNS AND SIZE INFORMATION

Scherrer's formula[21] is the best-known method for extracting size information from powder patterns (namely, from the Bragg peaks' width). This is a simple method, but accurate only to the order of magnitude. However, since Scherrer's work, line profile analysis has made enormous progress.[22–31]

Theoretical progress on understanding the physical origin of peak broadening has been focused on dislocation analysis, size broadening being considered as a side effect to be corrected for in order to determine the defect structure. Nevertheless, today it is possible to determine the parameters of a (log-normal) size distribution of crystallites, together with information on type and concentration of dislocations. These methods are, however, complex and sophisticated, requiring a fairly high signal-to-noise ratio, low and flat background, a precise deconvolution of the instrumental broadening, and especially well-isolated Bragg peaks.

Full-pattern fitting methods (cf. Sec. II A) are more direct and robust, especially when the target is the size analysis. First, they use all the experimental information, regardless of partial or total peak overlap, increasing redundancy and therefore precision and decreasing experimental requirements. Furthermore, they allow the evaluation of a NP-characteristic feature, namely, the variation with size of the lattice parameter[10,11] (an effect that can be important below 20 nm). Corrections for texture, microabsorption, anisotropic elastic peak shifts, and instrumental broadening can also be implemented.

An efficient and precise method to evaluate NP diffraction patterns is needed to perform full-pattern fits. Hereafter we discuss the shape-based method[17–19] with a thorough analysis of its validity limits.

A. NP shape-based diffraction models

We briefly recall some methods for the calculation of the powder diffraction intensity for a NP with known periodic structure and definite size and shape. In the following the length of a vector $\boldsymbol{v}$ will be denoted by v. Accordingly, $\boldsymbol{q}$ will be the scattering vector of length $q=2\sin\theta/\lambda$, where θ is the scattering half angle and λ the incident wavelength; $\boldsymbol{h}$ will denote the scattering vector associated with a Bragg peak, its length being h. A NP occupies a geometrical region of space G. We recall[32,33] the definition of a shape function $S(\boldsymbol{r})$, such that $S(\boldsymbol{r})=1$ if $\boldsymbol{r}$ lies inside G, and $S(\boldsymbol{r})=0$ otherwise. We shall henceforth suppose that $S(-\boldsymbol{r})=S(\boldsymbol{r})$ so that its Fourier transform is real.

However, defining the shape of a crystal means also to describe what happens to the atoms on the surface. These are increasingly important at very small sizes. In fact, there are different ways of interpreting the action of $S(\boldsymbol{r})$, the most meaningful ones being (a) truncating sharply the scattering density (the electron density for x rays) at the surface;[32,33] (b) selecting all whole unit cells whose origins are in G and all whole atoms whose centers lie in the selected cells;[34] (c) selecting all whole atoms whose centers are in G. Useful illustrations are found in Fig. 1 of Ref. 17 [see Figs. 1(a), 1(c), and 1(d), respectively, for (a), (b), and (c)].[35] To evaluate the diffracted intensities, in cases (b) and (c), one may utilize the Debye function. In this way the chosen model is faithfully represented. It is possible, however, to proceed in a different way, that is, by the shape-function method. Accordingly, we first evaluate the scattering amplitude $A(\boldsymbol{q})$. The explicit expressions[17] are, for cases (a), (b), (c):

$$A^{\mathrm{a}}(\boldsymbol{q})=\sum_{\boldsymbol{h}\in\Lambda^*}\widetilde{S}(\boldsymbol{q}-\boldsymbol{h})F(\boldsymbol{h}), \tag{1}$$

$$A^{\mathrm{b}}(\boldsymbol{q})=\sum_{\boldsymbol{h}\in\Lambda^*}\widetilde{S}(\boldsymbol{q}-\boldsymbol{h})F(\boldsymbol{q}), \tag{2}$$

$$A^{\mathrm{c}}(\boldsymbol{q})=\sum_{\boldsymbol{h}\in\Lambda^*}\widetilde{S}(\boldsymbol{q}-\boldsymbol{h})F(\boldsymbol{h},q), \tag{3}$$

where Λ^* is the reciprocal lattice; $\widetilde{S}(\boldsymbol{q})$ is the Fourier transform[36] of $S(\boldsymbol{r})$, or

$$\widetilde{S}(\boldsymbol{q})=\int_{\mathbb{R}^3}d^3\boldsymbol{r}\,S(\boldsymbol{r})e^{2\pi i\boldsymbol{q}\cdot\boldsymbol{r}}=\int_G d^3\boldsymbol{r}\,e^{2\pi i\boldsymbol{q}\cdot\boldsymbol{r}}, \tag{4}$$

and it satisfies $\widetilde{S}(\boldsymbol{q})=\widetilde{S}(-\boldsymbol{q})$ because $S(-\boldsymbol{r})=S(\boldsymbol{r})$; $F(\boldsymbol{h})$ is the unit-cell structure factor

$$F(\boldsymbol{h})=\sum_{\alpha=1}^{N_a}f_\alpha(h)e^{2\pi i\boldsymbol{h}\cdot\boldsymbol{r}_\alpha}, \tag{5}$$

where the sum index α runs over the atoms in the unit cell, which have form factors f_α,[37] and position vectors (relative to the cell origin) $\boldsymbol{r}_\alpha$; $F(\boldsymbol{q})$ is the same as the former but evaluated in $\boldsymbol{q}$; and $F(\boldsymbol{h},q)$ is the mixed expression

$$F(\boldsymbol{h},q)=\sum_{\alpha=1}^{N_a}f_\alpha(q)e^{2\pi i\boldsymbol{h}\cdot\boldsymbol{r}_\alpha}. \tag{6}$$

It is evident that form (a) is simpler but by construction less reasonable—for electron and x-ray diffraction—than (b) and (c). In fact, the sharp truncation of the electron density at the surface is unjustified. For neutron nuclear elastic scattering the atoms are point scatterers (when the Debye-Waller factor can be neglected or factored out); therefore, construction (a) coincides with (c). Accordingly, in the neutron case, the atomic form factors are constant and $A^{\mathrm{a}}(\boldsymbol{q})=A^{\mathrm{c}}(\boldsymbol{q})$.

Form (b) depends on an appropriate choice of the unit cell. Clearly, it preserves the stoichiometric composition and symmetry.

Form (c) needs a careful implementation (regarding the definition of G) to preserve stoichiometry, which is important for ionic compounds; however, it is clearly more flexible. Remark also that, in the case of monatomic lattices, instead—as for simple-cubic, face-centered or body-centered cubic metals—constructions (b) and (c) will be coincident and $A^{\mathrm{b}}(\boldsymbol{q})=A^{\mathrm{c}}(\boldsymbol{q})$.

B. NP scattering intensities

Squaring Eqs. (1)–(3) we obtain the intensities. Supposing S centrosymmetric and $\widetilde{S}$ real, we have

$$I^{\mathrm{a}}(\boldsymbol{q})=\sum_{\boldsymbol{h}\in\Lambda^*}\widetilde{S}^2(\boldsymbol{q}-\boldsymbol{h})|F(\boldsymbol{h})|^2, \tag{7}$$

$$I^{\mathrm{b}}(\boldsymbol{q})=|F(\boldsymbol{q})|^2\sum_{\boldsymbol{h}\in\Lambda^*}\widetilde{S}^2(\boldsymbol{q}-\boldsymbol{h}), \tag{8}$$

$$I^{\mathrm{c}}(\boldsymbol{q})=\sum_{\boldsymbol{h}\in\Lambda^*}\widetilde{S}^2(\boldsymbol{q}-\boldsymbol{h})|F(\boldsymbol{h},q)|^2. \tag{9}$$

Here, we have neglected cross summations of the form

$$\mathcal{R}(\boldsymbol{q})=\sum_{\substack{\mathbf{h},\mathbf{k}\in\Lambda^*\\ \mathbf{k}\neq\boldsymbol{h}}}\widetilde{S}(\boldsymbol{q}-\boldsymbol{h})\widetilde{S}(\boldsymbol{q}-\boldsymbol{k})M^{\mathrm{x}}_{\boldsymbol{q},\boldsymbol{h}}\bar{M}^{\mathrm{x}}_{\boldsymbol{q},\boldsymbol{k}} \tag{10}$$

where the overbar stands for the complex conjugate and, for $x=a,b,c$, respectively, it is $M^{\mathrm{a}}_{\boldsymbol{q},\boldsymbol{h}}=F(\boldsymbol{h})$, $M^{\mathrm{b}}_{\boldsymbol{q},\boldsymbol{h}}=F(\boldsymbol{q})$, or $M^{\mathrm{c}}_{\boldsymbol{q},\boldsymbol{h}}=F(\boldsymbol{h},q)$. Neglecting $\mathcal{R}(\boldsymbol{q})$ is, first of all, a question of convenience, because its evaluation—either analytical or numerical—is extremely difficult.

There are obvious reasons for neglecting $\mathcal{R}(\boldsymbol{q})$ for large particles. Consider a spherical particle with cubic structure with lattice parameter a and radius $R\gg a$. $\widetilde{S}(\boldsymbol{q})$ is large only for $q\lesssim 1/R$, and decreases as $(2\pi qR)^{-2}$ for $q\gg 1/R$. As for any Bragg peak $\boldsymbol{h}$ it is $1/R\ll 1/a\lesssim h$, $\mathcal{R}(\boldsymbol{q})\sim O((R/a)^{-2})$ can be neglected.

For smaller particles the situation is different. In Refs. 17 and 34 it is proposed that $\mathcal{R}(\boldsymbol{q})$ is negligible due to a certain statistical "smearing" of the NP surface region on a thickness of the order of the lattice parameter a. However, this hypothesis cannot be accepted by default.

First, the order at the surface strongly depends on the considered crystal phase and on the actual sample. Consider that for a NP of diameter $D=Na$, the fraction of atoms included in a layer of thickness a is $\approx 6/N$ (about 50% at $D=10a$ and still 12% at $D=50a$). The structure of this large fraction should be carefully considered on a case-by-case basis. Relaxations in the core due to a disordered layer of thickness a should also be considered. Second, supposing a default smearing of the NP boundaries flattens the different construction principles of forms (a), (b), and (c). In fact, the differences among them regard the finest details of the NP surface structure.

We shall hereafter assess the effect of neglecting $\mathcal{R}(\boldsymbol{q})$ on the calculation of a powder diffraction pattern. In the Appendix we carry out some relevant calculations. Evidently this will depend on the choice of form (a), (b), or (c). Examples are reported in the following section.

For form $I^{\mathrm{b}}(\boldsymbol{q})$ it turns out that, even when $\mathcal{R}(\boldsymbol{q})$ is not negligible, it yields a contribution that is approximately proportional to the retained term $I^{\mathrm{b}}(\boldsymbol{q})$ of the scattered intensity. This means that the effect of neglecting $\mathcal{R}(\boldsymbol{q})$ may be just a small error on the global scale factor for samples composed of particles of equal size. However, as this effect is size dependent, it may hamper the evaluation of size distribution when this is not very narrow. A size-related correction factor for the scale factor may—and should—be evaluated (see the Appendix) in this case. This of course is an undesired complication.

In cases (a) and (c) the neglected term $\mathcal{R}(\boldsymbol{q})$ depends on the crystal structure (see the Appendix). It is not a constant scale factor for all Bragg peaks, and it may have a significant gradient in the Bragg peak positions. At very small sizes the latter may induce a systematic error also in the lattice constant determination. However, in the x-ray case, for form (a) $\mathcal{R}(\boldsymbol{q})$ is larger—and has a larger gradient in the Bragg peak neighborhood—than the corresponding term for form (c).

C. NP powder patterns

To obtain a powder diffraction pattern, we must integrate $I^{x}(\boldsymbol{q})$ [x=a,b,c; see Eqs. (1)–(3)] at constant q. We write $\boldsymbol{q}$ in polar coordinates as $\boldsymbol{q}=(q\sin\psi\cos\phi, q\sin\psi\sin\phi, q\cos\psi)\equiv(q,\omega)$, where ω is the orientation defined by the pair (ψ,ϕ). We have to integrate over the set of all orientations $\Omega\equiv\{0<\psi<\pi, 0<\phi<2\pi\}$ (with $d\omega\equiv\sin\psi\, d\psi\, d\phi$), as

$$\sin\psi\, d\psi\int_0^{2\pi} d\phi\, I_p^{\mathrm{x}}(q) = q^2\int_\Omega d\omega\, I^{\mathrm{x}}(q,\omega). \tag{11}$$

In detail, considering the expressions for the different cases, we have

$$I_p^{\mathrm{a}}(q) = q^2\sum_{\boldsymbol{h}\in\Lambda^*}|F(\boldsymbol{h})|^2\int_\Omega d\omega\,\widetilde{S}^2(\boldsymbol{q}-\boldsymbol{h}), \tag{12}$$

$$I_p^{\mathrm{b}}(q) = q^2\sum_{\boldsymbol{h}\in\Lambda^*}\int_\Omega d\omega|F(\boldsymbol{q})|^2\widetilde{S}^2(\boldsymbol{q}-\boldsymbol{h}), \tag{13}$$

$$I_p^{\mathrm{c}}(q) = q^2\sum_{\boldsymbol{h}\in\Lambda^*}|F(\boldsymbol{h},q)|^2\int_\Omega d\omega\,\widetilde{S}^2(\boldsymbol{q}-\boldsymbol{h}). \tag{14}$$

The integration in case (b) is much more difficult and it cannot generally be expressed in closed form even for simple shapes. Therefore, as a careful implementation of form (c) is at least as good a description as form (b), we shall disregard (b) in the following. Suppose now that G is a sphere of radius R and volume $V=4\pi R^3/3$, we have

$$\widetilde{S}(\boldsymbol{q}) = \widetilde{S}(q) = 3V\left[\frac{\sin(y)-y\cos(y)}{y^3}\right]_{y=2\pi qR} \tag{15}$$

and, as $|\boldsymbol{q}-\boldsymbol{h}|=(q^2+h^2-2qh\cos\psi)^{1/2}$,

$$\widetilde{S}(\boldsymbol{q}-\boldsymbol{h}) = 3V\left[\frac{\sin(y)-y\cos(y)}{y^3}\right] \tag{16}$$

with $y=2\pi(q^2+h^2-2qh\cos\psi)^{1/2}R$.

Substituting in Eqs. (12) and (14) yields[32]

$$I_p^{\mathrm{a}}(q) = \frac{3qVR}{8\pi}\sum_{\boldsymbol{h}\in\Lambda^*}|F(\boldsymbol{h})|^2\frac{(A_- - A_+)}{h}, \tag{17}$$

$$I_p^{\mathrm{c}}(q) = \frac{3qVR}{8\pi}\sum_{\boldsymbol{h}\in\Lambda^*}|F(\boldsymbol{h},q)|^2\frac{(A_- - A_+)}{h}, \tag{18}$$

where $A_\pm\equiv y_\pm^{-2}[1-\sin(2y_\pm)/y_\pm+\sin^2(y_\pm)/y_\pm^2]$ for $y_\pm=2\pi R(q\pm h)$. Now we consider the crystal's Laue group $\mathcal{G}$ so that we can extend the summation on the asymmetric part $\Lambda^*/\mathcal{G}$ of the reciprocal lattice:

$$I_p^{\mathrm{a}}(q) = \frac{3qVR}{8\pi}\sum_{\boldsymbol{h}\in\Lambda^*/\mathcal{G}}\mu_{\boldsymbol{h}}|F(\boldsymbol{h})|^2\frac{(A_- - A_+)}{h}, \tag{19}$$

$$I_p^{\mathrm{c}}(q) = \frac{3qVR}{8\pi}\sum_{\boldsymbol{h}\in\Lambda^*/\mathcal{G}}\mu_{\boldsymbol{h}}|F(\boldsymbol{h},q)|^2\frac{(A_- - A_+)}{h}, \tag{20}$$

where $\mu_{\boldsymbol{h}}$ is the multiplicity of $\boldsymbol{h}$ subject to $\mathcal{G}$. Evaluation of $I_p^{\mathrm{c}}(q)$ is only slightly more complex than for $I_p^{\mathrm{a}}(q)$, and the gain in accuracy justifies the effort.

We have computed test patterns to compare forms (a) and (c), considering NPs of diameter $\approx 10a$, this being the lower size limit of validity of the shape-based approach.

We have considered Au_{3925} spherical fcc NPs of diameter 5 nm ($a=0.407\,86$ nm), constructed according to principle (c) of Sec. II A. The diffraction pattern has been evaluated for wavelength $\lambda=0.154\,056$ nm, $2\theta=20°$–$150°$, including Lorentz correction and Debye-Waller factor $\exp(-Bq^2/2)$ ($B=0.005$ nm^2). In this case, as the monatomic fcc Wigner-Seitz unit cell contains one atom, principle (c) coincides with (b). The powder pattern was calculated exactly by the Debye sum[10,15] and by Eqs. (19) and (20). The profiles shown in Fig. 1(a) have been calculated on an absolute scale. They match quite well, but a maximum error $\approx$2–3 % is present in both cases (a) and (c). The profile wR agreement index between I_p^{Debye} and I_p^{c} is 3.1%, between I_p^{Debye} and I_p^{a} is $wR=4.4\%$. The difference profiles [Fig. 1(b)] show that $I_p^{\mathrm{Debye}}-I_p^{\mathrm{c}}$ has a similar shape to I_p^{Debye}, while $I_p^{\mathrm{Debye}}-I_p^{\mathrm{a}}$ is quite

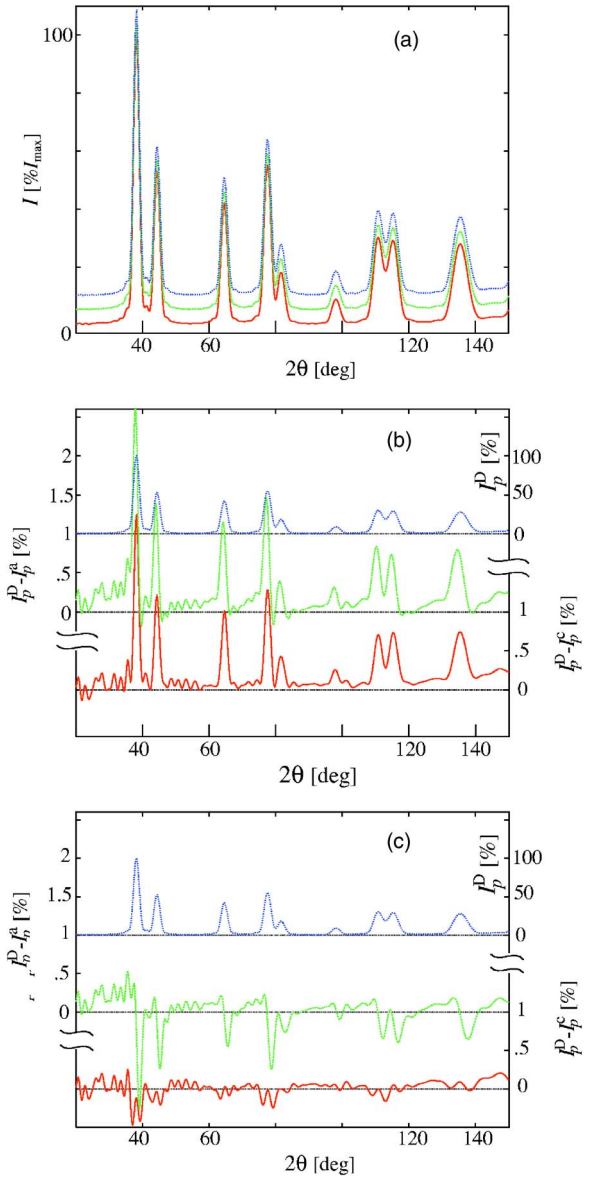

FIG. 1. (Color online) A model 5.0-nm spherical Au cluster. (a) The powder diffraction pattern. Continuous (red) line, exact intensity I_p^D calculated by the Debye function (Ref. 15); dashed (green) line, 5% shifted up, I_p^c, see Eq. (20); dotted (blue) line, 10% shifted up, I_p^a, see Eq. (19). All intensities are on the same scale and plotted as percent of max(I_p^D). (b) Bottom line (red), difference $I_p^D - I_p^c$; middle line (green), difference $I_p^D - I_p^a$; top line (blue), the exact pattern $I^D/100$ for comparison. (c) Bottom line, continuous (red), difference $I_p^D - s\, I_p^c$ after refining with a scale factor $s=1.024$; middle line, dashed (green), difference $I_p^D - sI_p^a$ after refining with a scale factor $s=1.027$; top line, dotted (blue), the exact pattern $I^D/100$ for comparison.

different. Accordingly, refining a scale factor between I_p^{Debye} and I_p^c lowers wR to 2.0% [with featureless difference, Fig. 1(c)], while a scale factor between I_p^{Debye} and I_p^a yields $wR=3.5\%$, with still a characteristic difference profile. Furthermore, the peak positions are very little shifted ($<0.002°$) between I_p^{Debye} and I_p^c, while they are shifted up to 0.04° between I_p^{Debye} and I_p^a.

Then, we considered $(ZnSe)_{1289}$ spherical NPs of diameter 4.8 nm of zinc-blende structure ($a=0.5633$ nm), constructed according to principle (c) of Sec. II A. The diffraction pattern has been evaluated for wavelength $\lambda=0.154056$ nm, $2\theta=20°-135°$, including Lorentz correction and Debye-Waller factor $\exp(-Bq^2/2)$ ($B=0.005$ nm^2). In this case, as the fcc Wigner-Seitz unit cell contains two atoms, construction (c) differs from (b). Once more, the powder pattern has been calculated exactly by the Debye sum[10,15] and also by Eqs. (19) and (20). The profiles—calculated on an absolute scale [Fig. 2(a)]- match with a maximum error ≈1–2 % for both cases (a) and (c). The profile agreement index wR between I_p^{Debye} and I_p^c is 1.8%, between I_p^{Debye} and I_p^a is $wR=3.1\%$. The difference profiles [Fig. 2(b)] show again that $I_p^{Debye}-I_p^c$ has a similar shape to I_p^{Debye}, while $I_p^{Debye}-I_p^a$ is quite different. Accordingly, we have refined again a scale factor (and this time also a different Debye-Waller factor B, assumed the same for Zn and Se) between I_p^{Debye} and I_p^c. wR decreases to 1.6% with featureless difference [Fig. 2(c)]. In contrast, when refining the scale factor and Debye-Waller factor between I_p^{Debye} and I_p^a the agreement index does not go below $wR=3.1\%$. Also the difference profile is little changed [Fig. 2(c)]. Again, the peak positions are very little shifted ($<0.001°$) between I_p^{Debye} and I_p^c, while peak shifts up to 0.05° between I_p^{Debye} and I_p^a are found. Form (c) again turns out to be less affected than (a) by neglecting the cross term $\mathcal{R}$. A small variation of the Debye-Waller factor (from 0.005 to 0.0047 nm^2) is due to the fact that the error due to neglect of $\mathcal{R}$ changes the intensity ratios slightly. This is however less troublesome than the peak shifts observed for form (a).

It results that at NP diameters $D\approx 10a$ the errors in the shape-based diffraction pattern calculations, whatever form we choose, start to be evident. This approach should not be used below this threshold. Also, form (a)—which is the standard choice for large particles—shows a much larger error and should be avoided in favor of (c).

D. The log-normal size distribution

There are several experimental and theoretical reasons[38] to believe that NP powders have a log-normal distribution of NP size. The log-normal distribution of NP radii is usually written in terms of its mode R_m and width w_R, as

$$L(R)=\frac{1}{w_R\sqrt{2\pi}}\exp\left\{-\frac{[\log(R)-\log(R_m)]^2}{2w_R^2}\right\}. \qquad (21)$$

The most direct information on a distribution is provided by the distribution-averaged NP radius R_{av} and the relevant standard deviation σ_R. For a log-normal distribution, the latter parameters are related to the former by

$$R_{av}=R_m\exp(w_R^2/2), \quad \sigma_R=R_m^2\exp(2w_R^2), \qquad (22)$$

and

$$R_m=\frac{1}{\sqrt{1+\sigma_R^2/R_{av}^2}},$$

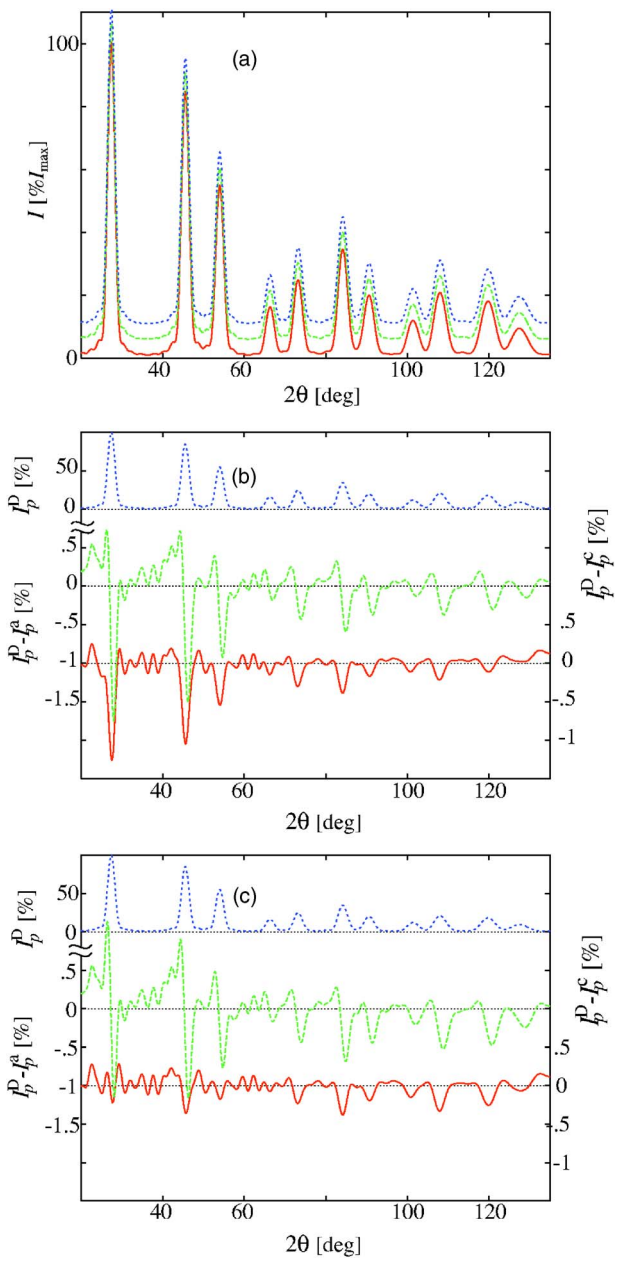

FIG. 2. (Color online) A model 4.8-nm cubic ZnSe spherical NP. (a) The powder diffraction pattern. Continuous (red) line, exact intensity I_p^D calculated by the Debye function (Ref. 15); dashed (green) line, 5% shifted up, I_p^c, see Eq. (20); dotted (blue) line, 10% shifted up, I_p^a, see Eq. (19). All intensities are on the same relative scale, as percent of max(I_p^{Debye}). (b) Bottom line (red), difference $I_p^D - I_p^c$; middle line (green), difference $I_p^D - I_p^a$; top line (blue), the exact pattern $I^D/100$ for comparison. (c) Bottom line (red), difference $I_p^D - sI_p^c$ after refining with a scale factor $s=0.999$ and an overall-isotropic Debye-Waller factor $B=0.468$; middle line (green), difference $I_p^D - sI_p^a$ after refining with a scale factor $s=0.996$ and $B=0.467$; top line (blue), the exact pattern $I^D/100$ for comparison.

$$w_R = \sqrt{\log(1+\sigma_R^2/R_{av}^2)}. \tag{23}$$

We shall use a form depending directly on R_{av}, σ_R.[39] Setting two adimensional parameters $\rho = R/R_{av}$, $c = 1+\sigma_R^2/R_{av}^2$, we have

$$L(R) = \frac{1}{R\sqrt{2\pi\log(c)}} \exp\left[-\frac{\log^2(\rho\sqrt{c})}{2\log(c)}\right]. \tag{24}$$

Volume- and area-averaged NP diameters can be derived from

$$D_V = \frac{3}{2}R_{av}c^3, \quad D_A = \frac{4}{3}R_{av}c^2. \tag{25}$$

III. NANOCRYSTALLINE CERIA

A. Experiment

X-ray powder diffraction patterns of a nanocrystalline 20-nm CeO_2 sample, available for a round robin,[39] were downloaded.[40] The NP size is well inside the limits of validity of the shape-based method. Among the available data sets, the selected raw data were collected at the NSLS X3B1 beamline of the Brookhaven National Laboratory in flat-plate geometry, with a double-crystal Si(111) monochromator on the incident beam [$\lambda = 0.6998$ Å, $2\theta = 12°(0.01°)60°$] and a Ge(111) analyzer crystal on the diffracted beam.

B. Data preprocessing

Three data preprocessing stages have been accomplished. First, the instrumental function has been deconvoluted by an original advanced technique, including denoising and background subtraction, described in Ref. 41.

Second, the pattern has been fitted by generic asymmetric Voigt profiles so as to obtain information about peak positions and intensities. By comparing the intensities as evaluated from the fit with the theoretical ones a small correction for texture and/or microabsorption has been evaluated. The intensity corrections so obtained have then been stored and used in the subsequent stages.

Finally, the peak positions were found to be slightly anisotropically shifted. This has been attributed to a small residual stress, due, e.g., to dislocations. To confirm this point, we have evaluated the average lattice spacing variations $[\Delta d/d]_{\boldsymbol{h}} = -(\pi/360)\cot(\theta_{\boldsymbol{h}})\Delta(2\theta_{\boldsymbol{h}})$ for all single reflections $\boldsymbol{h}$. Then we have compared those values with a simple model of elastic anisotropy.[42] They resulted in good agreement. In Fig. 3 we show the fit of $[\Delta d/d]_{\boldsymbol{h}}$'s with Eq. (28) of Ref. 42. The magnitudes of the residual stress tensor components, at least for those which can be determined in this way, resulted in the range 1–10 MPa. The values of $|\Delta(2\theta_{\boldsymbol{h}})|$ are below 0.005°, and $[\Delta d/d]_{\boldsymbol{h}}$ are in the range in $(1–7)\times 10^{-4}$, which are quite small values. As the strain broadening is of the same order of magnitude as the peak shifts,[43] we can confirm that strain broadening is rather small in the CeO_2 sample and can be neglected, as in Ref. 39. Also the residual-stress peak shifts so obtained have been saved as fixed corrections for the subsequent stages.

C. Full-pattern refinement

The total intensity diffracted by the powder NP sample is described by the sum

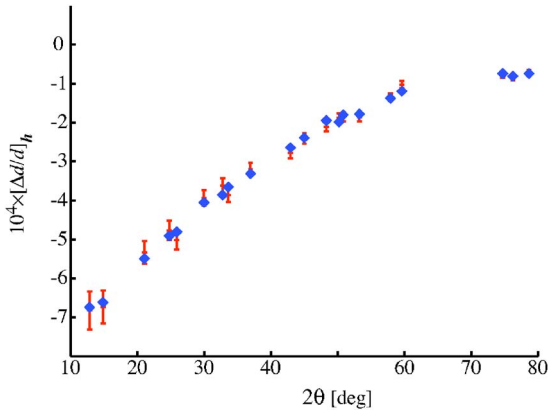

FIG. 3. (Color online) The measured (red, error bars) and calculated (blue, diamonds) lattice spacing variations for all well-isolated Bragg peaks of CeO_2 plotted against the relevant peak diffraction angles. Error bars have been evaluated assuming a constant error of 0.0006° on the anisotropic angular peak shift. Calculated values refer to the model of Ref. 42 where residual stress components have been refined.

$$I^{cal}(q) = I^{bkg}(q) + \sum_{k=0}^{k_{max}} L(R_k) I_k(q), \tag{26}$$

where $R_k=(k+1/2)\Delta R$, $k=1-k_{max}$; $I_k(q)$ is $I_p^c(q)$ of Eq. (20) evaluated at $R=R_k$; and $I^{bkg}(q)$ is a polynomial modeling the background. The step $\Delta R=a(2\pi/3)^{-1/3}$ is chosen so as to have an integer number of atoms in each kth sphere of radius R_k, while keeping the point density constant and preserving stoichiometry. It is evidently possible to use a size-dependent lattice parameter a_k in the calculation of $I_k(q)$. For this sample this has been deemed unnecessary. Indeed, for diameters of 20 nm, the lattice parameter of CeO_2 has been found[44] to be already equal to the bulk value. A least-squares full-pattern refinement means minimizing the quantity

$$\chi^2 = \sum_{i=1}^{N_{obs}} [I^{cal}(q_i) - I_i^{obs}]^2 w_i. \tag{27}$$

Here I_i^{obs} is the ith point of the experimental pattern corresponding to the scattering vector q_i, N_{obs} is the number of experimental points, and the weights w_i are the estimated inverse variance of the observations. The refined parameters are the average NP radius (R_{av}) and the radius dispersion σ_R, the isotropic Debye-Waller factors B for O and Ce atoms, the cubic unit-cell parameter a, and seven background coefficients. For the minimization, we have used (for this work) a modified simplex algorithm,[45] which is robust but time consuming; however, computing times were reasonable. A derivative-based algorithm (Newton, in progress) should give a handsome acceleration.

The final results are given in Table. I, together with the corresponding values of Ref. 39. The Debye-Waller factors result as $B_{Ce}=0.0065$ nm^2 and $B_O=0.0084$ nm^2. The calculated profile is plotted in Fig. 4 with the experimental pattern and the profile difference. The excellent fit quality and the final goodness-of-fit value (1.21) indicate the achievement of a reliable result. Indeed, the estimated parameters are in good agreement with Ref. 39. The slight discrepancy (≈0.2 nm), larger than the standard deviations, might be explained by the improved deconvolution method here applied and by the use of the whole pattern instead of a limited number of peaks as in Ref. 39.

TABLE I. Comparison of size distribution results. Standard deviations are in parentheses. Units are nanometers, except for σ_R^2/R_{av}^2, which is adimensional.

	This work	Ref. 39
R_{av}	9.58 (0.02)	9.33 (0.07)
σ_R	4.138 (0.003)	3.92
σ_R^2/R_{av}^2	0.1866 (0.0008)	0.177 (0.003)
D_V	24.01 (0.02)	22.8 (0.4)
D_A	17.98 (0.02)	17.2 (0.2)

IV. CONCLUSIONS

The method of shape convolution to calculate the diffraction pattern of NP powders has been thoroughly discussed with respect to its limits of validity. Concerns in applying this method below its optimal size range have been demonstrated theoretically and by simulated patterns. Finally, the effectiveness of full-pattern powder data analysis based on the shape-convolution method was proved in obtaining precise size distribution information on NP powder samples with a log-normal distribution of spherical crystallites.

APPENDIX: ERROR EVALUATION

Assume we deal with particles of centrosymmetric shape $S(\boldsymbol{r})=S(-\boldsymbol{r})$ and equivalent spherical radius R (i.e., the radius

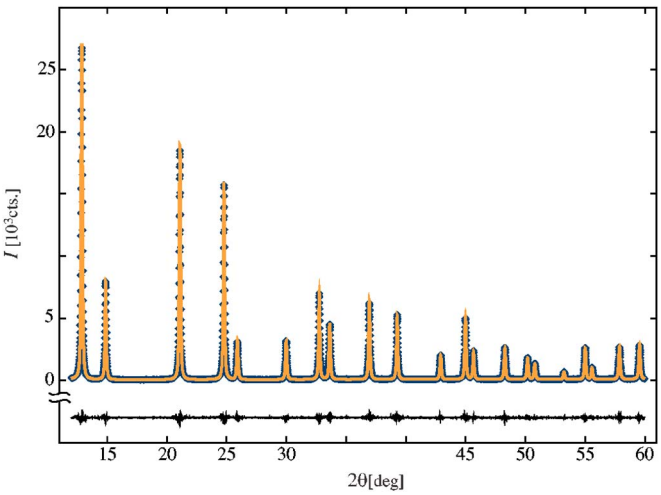

FIG. 4. (Color online) Nanosized CeO_2 powder pattern final fit. Violet Dark gray (violet) diamonds, the observed deconvoluted intensity; light gray (orange) thick line, the calculated intensity; black thin line, below, difference profile (same scale, shifted).

of the sphere of equal volume). The shape Fourier transform $\tilde{S}(\boldsymbol{q})$ is then a real even function:

$$\tilde{S}(\boldsymbol{q}) = \tilde{S}(-\boldsymbol{q}). \tag{A1}$$

Recall also that the gradient of an even function is odd:

$$\tilde{\boldsymbol{G}}(\boldsymbol{q}) \equiv \boldsymbol{\nabla}_{\boldsymbol{q}}\tilde{S}(\boldsymbol{q}) = -\tilde{\boldsymbol{G}}(-\boldsymbol{q}). \tag{A2}$$

Our aim is to evaluate—for the different forms (a), (b), (c) as introduced in Sec. II A and calculated in Secs. II B and II C—the neglected residual intensity contribution $\mathcal{R}(\boldsymbol{q})$ of Eq. (10) with respect to the corresponding retained term [cf. Eqs. (7)–(9)] in the immediate vicinity of a Bragg peak.

Let $\boldsymbol{h}_0$ be the nearest Bragg peak to $\boldsymbol{q}$. First note that, if $|\boldsymbol{q}-\boldsymbol{h}_0| \gg 1/R$, $\mathcal{R}(\boldsymbol{q})$ is of order $(2\pi qR)^{-4}$, so we neglect it altogether. If $\boldsymbol{q}$ is very close to $\boldsymbol{h}_0$, set $\boldsymbol{q}=\boldsymbol{h}_0+\Delta\boldsymbol{q}$ (so $\Delta q \lesssim 1/R$). We can drop in the sum over $\boldsymbol{h}$ all terms with $\boldsymbol{h} \neq \boldsymbol{h}_0$ because they are $O(2\pi qR)^{-4}$ and reorder the second sum, obtaining

$$\mathcal{R}^{\mathrm{a}}(\boldsymbol{h}_0+\Delta\boldsymbol{q}) \approx \tilde{S}(\Delta\boldsymbol{q}) \sum_{\substack{\boldsymbol{k}\in\Lambda^* \\ \boldsymbol{k}\neq\boldsymbol{0}}} \tilde{S}(\Delta\boldsymbol{q}+\boldsymbol{k})F(\boldsymbol{h}_0)\bar{F}(\boldsymbol{h}_0-\boldsymbol{k}), \tag{A3}$$

$$\mathcal{R}^{\mathrm{b}}(\boldsymbol{h}_0+\Delta\boldsymbol{q}) \approx \tilde{S}(\Delta\boldsymbol{q})|F(\boldsymbol{h}_0+\Delta\boldsymbol{q})|^2 \sum_{\substack{\boldsymbol{k}\in\Lambda^* \\ \boldsymbol{k}\neq\boldsymbol{0}}} \tilde{S}(\Delta\boldsymbol{q}+\boldsymbol{k}), \tag{A4}$$

$$\mathcal{R}^{\mathrm{c}}(\boldsymbol{h}_0+\Delta\boldsymbol{q}) \approx \tilde{S}(\Delta\boldsymbol{q}) \sum_{\substack{\boldsymbol{k}\in\Lambda^* \\ \boldsymbol{k}\neq\boldsymbol{0}}} \tilde{S}(\Delta\boldsymbol{q}+\boldsymbol{k})F(\boldsymbol{h}_0,q)\bar{F}(\boldsymbol{h}_0-\boldsymbol{k},q), \tag{A5}$$

where $q \equiv |\boldsymbol{h}_0+\Delta\boldsymbol{q}|$.

At the same time, for $\boldsymbol{q}=\boldsymbol{h}_0+\Delta\boldsymbol{q}$ with $\Delta q \lesssim 1/R$, the intensities $I^{\mathrm{x}}(\boldsymbol{q})$ of Eqs. (7)–(9) can be approximated by the $\boldsymbol{h}_0$th term of the sum on the right-hand side, neglecting terms of $O(2\pi qR)^{-4}$. Furthermore, in general, $\tilde{S}(\Delta\boldsymbol{q})=\tilde{S}(0)+O(\Delta q^2)$. Therefore, the ratios $\mathcal{R}^{\mathrm{x}}(\boldsymbol{h}_0+\Delta\boldsymbol{q})/I^{\mathrm{x}}(\boldsymbol{h}_0+\Delta\boldsymbol{q})$ are given by

$$\hat{\mathcal{R}}^{\mathrm{a}}(\boldsymbol{h}_0,\Delta\boldsymbol{q}) \equiv \frac{\mathcal{R}^{\mathrm{a}}(\boldsymbol{h}_0+\Delta\boldsymbol{q})}{\tilde{S}^2(\Delta\boldsymbol{q})|F(\boldsymbol{h}_0)|^2} \approx \sum_{\substack{\boldsymbol{k}\in\Lambda^* \\ \boldsymbol{k}\neq\boldsymbol{0}}} \tilde{s}(\Delta\boldsymbol{q},\boldsymbol{k})\frac{\bar{F}(\boldsymbol{h}_0-\boldsymbol{k})}{\bar{F}(\boldsymbol{h}_0)}, \tag{A6}$$

$$\hat{\mathcal{R}}^{\mathrm{b}}(\boldsymbol{h}_0,\Delta\boldsymbol{q}) \equiv \frac{\mathcal{R}^{\mathrm{b}}(\boldsymbol{h}_0+\Delta\boldsymbol{q})}{\tilde{S}^2(\Delta\boldsymbol{q})|F(\boldsymbol{h}_0+\Delta\boldsymbol{q})|^2} \approx \sum_{\substack{\boldsymbol{k}\in\Lambda^* \\ \boldsymbol{k}\neq\boldsymbol{0}}} \tilde{s}(\Delta\boldsymbol{q},\boldsymbol{k}), \tag{A7}$$

$$\hat{\mathcal{R}}^{\mathrm{c}}(\boldsymbol{h}_0,\Delta\boldsymbol{q}) \equiv \frac{\mathcal{R}^{\mathrm{c}}(\boldsymbol{h}_0+\Delta\boldsymbol{q})}{\tilde{S}^2(\Delta\boldsymbol{q})|F(\boldsymbol{h}_0,q)|^2} \approx \sum_{\substack{\boldsymbol{k}\in\Lambda^* \\ \boldsymbol{k}\neq\boldsymbol{0}}} \tilde{s}(\Delta\boldsymbol{q},\boldsymbol{k})\frac{\bar{F}(\boldsymbol{h}_0-\boldsymbol{k},q)}{\bar{F}(\boldsymbol{h}_0,q)} \tag{A8}$$

where $\tilde{s}(\Delta\boldsymbol{q},\boldsymbol{k}) \equiv \tilde{S}(\Delta\boldsymbol{q}+\boldsymbol{k})/\tilde{S}(0)$.

Note that, because of Eqs. (A1) and (A2), we have

$$\tilde{s}(\Delta\boldsymbol{q},\boldsymbol{k}) = \tilde{s}(-\Delta\boldsymbol{q},-\boldsymbol{k}), \tag{A9}$$

$$\tilde{\boldsymbol{g}}(\Delta\boldsymbol{q},\boldsymbol{k}) \equiv \boldsymbol{\nabla}_{\Delta\boldsymbol{q}}\tilde{s}(\Delta\boldsymbol{q},\boldsymbol{k}) = \tilde{\boldsymbol{G}}(\Delta\boldsymbol{q}+\boldsymbol{k})/\tilde{S}(0) = -\tilde{\boldsymbol{g}}(-\Delta\boldsymbol{q},-\boldsymbol{k}). \tag{A10}$$

We can immediately verify that in case (b) the result is

$$\boldsymbol{\nabla}_{\Delta\boldsymbol{q}}\hat{\mathcal{R}}^{\mathrm{b}}(\boldsymbol{h}_0,\Delta\boldsymbol{q}) = \sum_{\substack{\boldsymbol{k}\in\Lambda^* \\ \boldsymbol{k}\neq\boldsymbol{0}}} \tilde{\boldsymbol{g}}(\Delta\boldsymbol{q},\boldsymbol{k}). \tag{A11}$$

In the sum above the term with index $\boldsymbol{k}$ is always accompanied by a term with index $-\boldsymbol{k}$. Setting also $\Delta\boldsymbol{q}=0$, and using Eq. (A10), we have

$$\boldsymbol{\nabla}_{\Delta\boldsymbol{q}}\hat{\mathcal{R}}^{\mathrm{b}}(\boldsymbol{h}_0,0) = \sum_{\boldsymbol{k}\in\Lambda^*/2} [\tilde{\boldsymbol{g}}(0,\boldsymbol{k}) + \tilde{\boldsymbol{g}}(0,-\boldsymbol{k})] = 0, \tag{A12}$$

where $\Lambda^*/2$ denotes an arbitrarily chosen half space of the reciprocal lattice without the origin. Now, expanding $\hat{\mathcal{R}}^{\mathrm{b}}(\boldsymbol{h}_0,\Delta\boldsymbol{q})$ in Taylor series at $\Delta\boldsymbol{q}=0$, we have

$$\hat{\mathcal{R}}^{\mathrm{b}}(\boldsymbol{h}_0,\Delta\boldsymbol{q}) \approx \hat{\mathcal{R}}^{\mathrm{b}}(\boldsymbol{h}_0,0) + O(\Delta q^2). \tag{A13}$$

Note also in Eq. (A7) that $\hat{\mathcal{R}}^{\mathrm{b}}(\boldsymbol{h}_0,0)$ does not depend on the considered Bragg reflection $\boldsymbol{h}_0$. Therefore, we can write

$$\mathcal{R}^{\mathrm{b}}(\boldsymbol{q}) \propto I^{\mathrm{b}}(\boldsymbol{q}), \tag{A14}$$

and the proportionality constant can be evaluated by Eq. (A7) with $\Delta\boldsymbol{q}=\boldsymbol{0}$. We can conclude that the effect of neglecting $\mathcal{R}^{\mathrm{b}}$ will be just a relative error on the global profile scale factor. This factor is size dependent, however, therefore for size distribution analysis at small sizes it may be necessary to introduce a correction as from Eq. (A7).

Cases (a) and (c), are more complex. We are interested in powder diffraction, where $I(\boldsymbol{q})$ is to be integrated at constant q; therefore we shall consider

$$\bar{\mathcal{R}}^{\mathrm{x}}(\boldsymbol{h}_0,\Delta\boldsymbol{q}) = \frac{1}{2}[\hat{\mathcal{R}}^{\mathrm{x}}(\boldsymbol{h}_0,\Delta\boldsymbol{q}) + \hat{\mathcal{R}}^{\mathrm{x}}(-\boldsymbol{h}_0,-\Delta\boldsymbol{q})]. \tag{A15}$$

Expanding $\bar{\mathcal{R}}^{\mathrm{x}}(\boldsymbol{h}_0,\Delta\boldsymbol{q})$ in Taylor series at $\Delta\boldsymbol{q}=\boldsymbol{0}$, we have

$$\bar{\mathcal{R}}^{\mathrm{x}}(\boldsymbol{h}_0,\Delta\boldsymbol{q}) \approx \bar{\mathcal{R}}^{\mathrm{x}}(\boldsymbol{h}_0,0) + \boldsymbol{\nabla}_{\Delta\boldsymbol{q}}\bar{\mathcal{R}}^{\mathrm{x}}(\boldsymbol{h}_0,0)\cdot\Delta\boldsymbol{q} + O(\Delta q^2). \tag{A16}$$

We shall now develop $\bar{\mathcal{R}}^{\mathrm{a}}(\boldsymbol{h}_0,\Delta\boldsymbol{q})$ and $\boldsymbol{\nabla}_{\Delta\boldsymbol{q}}\bar{\mathcal{R}}^{\mathrm{a}}(\boldsymbol{h}_0,0)$ in cases (a) and (c).

1. Case (c)

First, recall that the atomic form factors $f_\alpha(q)$ are constants for neutron scattering and monotonically decreasing

smooth functions in the x-ray case. In the latter case, furthermore, the form factors of different elements have remarkably similar profiles. For a structure with N_a atoms in the unit cell, it is then possible[46] to approximate

$$f_\alpha(q) \approx c_\alpha \langle f(q) \rangle \equiv c_\alpha \frac{1}{N_a} \sum_{\beta=1}^{N_a} f_\beta(q) \tag{A17}$$

with c_α appropriate constants. Therefore the structure factor ratios appearing in Eq. (A8) can be simplified as

$$\frac{\bar{F}(\boldsymbol{h}_0 - \boldsymbol{k}, q)}{\bar{F}(\boldsymbol{h}_0, q)} \approx \frac{\sum_{\alpha=1}^{N_a} c_\alpha e^{-2\pi i (\boldsymbol{h}_0 - \boldsymbol{k}) \cdot \boldsymbol{r}_\alpha}}{\sum_{\beta=1}^{N_a} c_\beta e^{-2\pi i \boldsymbol{h}_0 \cdot \boldsymbol{r}_\beta}} \equiv \tau(\boldsymbol{h}_0, \boldsymbol{k}), \tag{A18}$$

independent of $q = |\boldsymbol{h}_0 + \Delta \boldsymbol{q}|$. Note that

$$\tau(-\boldsymbol{h}_0, -\boldsymbol{k}) = \bar{\tau}(\boldsymbol{h}_0, \boldsymbol{k}), \quad \tau(-\boldsymbol{h}_0, \boldsymbol{k}) = \bar{\tau}(\boldsymbol{h}_0, -\boldsymbol{k}). \tag{A19}$$

Now we can write explicitly $\bar{\mathcal{R}}^{\mathrm{c}}$ using Eqs. (A8) and (A15) and

$$\bar{\mathcal{R}}^{\mathrm{c}}(\boldsymbol{h}_0, \Delta \boldsymbol{q}) = \frac{1}{2} \sum_{\substack{\boldsymbol{k} \in \Lambda^* \\ \boldsymbol{k} \neq \boldsymbol{0}}} [\tilde{s}(\Delta \boldsymbol{q}, \boldsymbol{k}) \tau(\boldsymbol{h}_0, \boldsymbol{k}) + \tilde{s}(-\Delta \boldsymbol{q}, \boldsymbol{k}) \bar{\tau}(\boldsymbol{h}_0, -\boldsymbol{k})]. \tag{A20}$$

Splitting the sum, reordering $\boldsymbol{k} \to -\boldsymbol{k}$ in one part, using Eq. (A9), and recombining, we have

$$\bar{\mathcal{R}}^{\mathrm{c}}(\boldsymbol{h}_0, \Delta \boldsymbol{q}) = \sum_{\substack{\boldsymbol{k} \in \Lambda^* \\ \boldsymbol{k} \neq \boldsymbol{0}}} \tilde{s}(\Delta \boldsymbol{q}, \boldsymbol{k}) \mathrm{Re}[\tau(\boldsymbol{h}_0, \boldsymbol{k})]. \tag{A21}$$

Again as in Eq. (A12), we can pair terms with $\boldsymbol{k}$ and $-\boldsymbol{k}$. Using Eq. (A19), we obtain

$$\bar{\mathcal{R}}^{\mathrm{c}}(\boldsymbol{h}_0, \Delta \boldsymbol{q}) = \sum_{\boldsymbol{k} \in \Lambda^*/2} \mathrm{Re}[\tilde{s}(\Delta \boldsymbol{q}, \boldsymbol{k}) \tau(\boldsymbol{h}_0, \boldsymbol{k}) + \tilde{s}(\Delta \boldsymbol{q}, -\boldsymbol{k}) \tau(\boldsymbol{h}_0, -\boldsymbol{k})]. \tag{A22}$$

Define now the arbitrary half lattice $\Lambda^*/2$ as that defined by a plane perpendicular to $\boldsymbol{h}_0$ passing through the origin and containing $\boldsymbol{h}_0$. The origin is excluded. We have

$$\bar{\mathcal{R}}^{\mathrm{c}}(\boldsymbol{h}_0, 0) = \sum_{\boldsymbol{k} \in \Lambda^*/2} \tilde{s}(0, \boldsymbol{k}) \mathrm{Re}[\tau(\boldsymbol{h}_0, \boldsymbol{k}) + \tau(\boldsymbol{h}_0, -\boldsymbol{k})]. \tag{A23}$$

Then, evaluating the gradient in $\Delta \boldsymbol{q} = \boldsymbol{0}$, using Eq. (A2), we have finally

$$\boldsymbol{\nabla}_{\Delta \boldsymbol{q}} \bar{\mathcal{R}}^{\mathrm{c}}(\boldsymbol{h}_0, 0) = \sum_{\boldsymbol{k} \in \Lambda^*/2} \tilde{\boldsymbol{g}}(0, \boldsymbol{k}) \mathrm{Re}[\tau(\boldsymbol{h}_0, \boldsymbol{k}) - \tau(\boldsymbol{h}_0, -\boldsymbol{k})]. \tag{A24}$$

The gradient $\boldsymbol{\nabla}_{\Delta \boldsymbol{q}} \bar{\mathcal{R}}^{\mathrm{c}}(\boldsymbol{h}_0, 0)$ is a vector. We have to take its angular average to determine the effect on the powder pattern. This is done by simply taking the scalar product with $\hat{\boldsymbol{h}}_0 \equiv \boldsymbol{h}_0 / h_0$:

$$\boldsymbol{\nabla}_{\Delta \boldsymbol{q}} \bar{\mathcal{R}}^{\mathrm{c}}(\boldsymbol{h}_0, 0) \cdot \hat{\boldsymbol{h}}_0 = \sum_{\boldsymbol{k} \in \Lambda^*/2} [\tilde{\boldsymbol{g}}(0, \boldsymbol{k}) \cdot \hat{\boldsymbol{h}}_0] \mathrm{Re}[\tau(\boldsymbol{h}_0, \boldsymbol{k}) - \tau(\boldsymbol{h}_0, -\boldsymbol{k})]. \tag{A25}$$

For a spherical shape, this will be $\tilde{\boldsymbol{g}}(0, \boldsymbol{k}) \| \boldsymbol{k}$; therefore terms with $\boldsymbol{k} \perp \boldsymbol{h}_0$ will be zero and those with $\boldsymbol{k} \| \boldsymbol{h}_0$ will be most important. Both $\tilde{\boldsymbol{g}}(0, \boldsymbol{k})$ and $\tilde{s}(0, \boldsymbol{k})$ are damped oscillatory functions with amplitude $\sim (2\pi k R)^{-2}$. As $1/a \lesssim k$, the magnitudes of both $\bar{\mathcal{R}}^{\mathrm{c}}(\boldsymbol{h}_0, 0)$ and $\boldsymbol{\nabla}_{\Delta \boldsymbol{q}} \bar{\mathcal{R}}^{\mathrm{c}}(\boldsymbol{h}_0, 0)$ are of order $(a/R)^2$. Unfortunately, Eq. (A25) cannot be estimated in more detail, because of the dependence on the "reduced" structure factors $\tau(\boldsymbol{h}_0, \boldsymbol{k})$. However, we can assess that its importance would be smaller than the corresponding term for case (a) for x-ray scattering.

2. Case (a)

In case (a), we can trace the same steps as in case (c) but instead of the reduced structure factors $\tau(\boldsymbol{h}_0, \boldsymbol{k})$ we have to consider the ratios

$$\zeta(\boldsymbol{h}_0, \boldsymbol{k}) = \frac{\bar{F}(\boldsymbol{h}_0 - \boldsymbol{k})}{\bar{F}(\boldsymbol{h}_0)} = \frac{\bar{F}(\boldsymbol{h}_0 - \boldsymbol{k}) F(\boldsymbol{h}_0)}{|F(\boldsymbol{h}_0)|^2} \tag{A26}$$

and in the analogous sums of Eq. (A23) and Eq. (A25) for $\bar{\mathcal{R}}^{\mathrm{a}}(\boldsymbol{h}_0, 0)$ and $\boldsymbol{\nabla}_{\Delta \boldsymbol{q}} \bar{\mathcal{R}}^{\mathrm{a}}(\boldsymbol{h}_0, 0)$ there will appear terms such as

$$\mathrm{Re}[\zeta(\boldsymbol{h}_0, \boldsymbol{k}) \pm \zeta(\boldsymbol{h}_0, -\boldsymbol{k})]. \tag{A27}$$

The most important terms for the powder pattern are again those with $\boldsymbol{k} \| \boldsymbol{h}_0$. The structure factors $F(\boldsymbol{h}_0 \pm \boldsymbol{k})$ [see Eq. (5)] depend on form factors $f_\alpha(|\boldsymbol{h}_0 \pm \boldsymbol{k}|)$, and for $\boldsymbol{k} \| \boldsymbol{h}_0$ these will be strongly different. This in turn will amplify the differences $\xi(\boldsymbol{h}_0, \boldsymbol{k})$. Therefore it is likely that for case (a) the effect of the neglected term $\mathcal{R}^{\mathrm{a}}$ will be significantly larger than for case (c). The examples reported in Sec. II C show just that.

*Permanent address: Consiglio Nazionale delle Ricerche, Istituto di Cristallografia (CNR-IC), Via Amendola 122/O, I-70126 Bari, Italy.
†Electronic address: cinzia.giannini@ic.cnr.it

[1] O. Masala and R. Seshadri, Annu. Rev. Mater. Res. **34**, 41 (2004).
[2] S. Ino, J. Phys. Soc. Jpn. **21**, 346 (1966).
[3] S. Ino and S. Ogawa, J. Phys. Soc. Jpn. **22**, 1365 (1967).
[4] S. Ino, J. Phys. Soc. Jpn. **26**, 1559 (1969).
[5] S. Ino, J. Phys. Soc. Jpn. **27**, 941 (1969).
[6] L. D. Marks, Rep. Prog. Phys. **57**, 603 (1994).
[7] W. Vogel, J. Bradley, O. Vollmer, and I. Abraham, J. Phys. Chem. B **102**, 10853 (1998).
[8] D. Zanchet, B. H. Hall, and D. Ugarte, J. Phys. Chem. B **104**, 11013 (2000).
[9] B. D. Hall, J. Appl. Phys. **87**, 1666 (2000).
[10] A. Cervellino, C. Giannini, and A. Guagliardi, J. Appl. Crystallogr. **36**, 1148 (2003).
[11] A. Cervellino, C. Giannini, A. Guagliardi, and D. Zanchet, Eur. Phys. J. B **41**, 485 (2004).
[12] B. Palosz *et al.*, Z. Kristallogr. **217**, 497 (2002).
[13] B. Palosz, E. Grzanka, S. Stel'makh, S. Gierlotka, R. Pielaszek, U. Bismayer, H. Weber, T. Proffen, and W. Palosz, Solid State Phenom. **94**, 203 (2003).
[14] B. Palosz, S. Stel'makh, E. Grzanka, S. Gierlotka, R. Pielaszek, U. Bismayer, S. Werner, and W. Palosz, J. Phys.: Condens. Matter **16**, S353 (2004).
[15] A. Guinier, *X-Ray Diffraction in Crystals, Imperfect Crystals, and Amorphous Bodies*, reprint ed. (Dover Publications, New York, 1994), Chap. 2, pp. 27-54.
[16] A. Cervellino, C. Giannini, and A. Guagliardi (unpublished).
[17] T. Ino and N. Minami, Acta Crystallogr., Sect. A: Cryst. Phys., Diffr., Theor. Gen. Crystallogr. **35**, 163 (1979).
[18] N. Minami and T. Ino, Acta Crystallogr., Sect. A: Cryst. Phys., Diffr., Theor. Gen. Crystallogr. **35**, 171 (1979).
[19] T. Ino and N. Minami, Acta Crystallogr., Sect. A: Found. Crystallogr. **40**, 538 (1984).
[20] Other NP samples (ZnTe, ZnSe) in the 5-20 nm size range have been treated successfully and the results will be published separately.
[21] P. Scherrer, Nachr. Ges. Wiss. Goettingen, Math.-Phys. Kl. **26**, 98 (1918).
[22] B. E. Warren and B. L. Averbach, J. Appl. Phys. **23**, 497 (1952).
[23] B. E. Warren, *X-Ray Diffraction* (Addison-Wesley, Menlo Park, CA, 1969).
[24] M. Wilkens, Phys. Status Solidi A **2**, 359 (1970).
[25] J. I. Langford and A. J. C. Wilson, J. Appl. Crystallogr. **11**, 102 (1978).
[26] T. Ungár, Á. Révész, and A. Borbély, J. Appl. Crystallogr. **31**, 554 (1998).
[27] J. I. Langford, D. Louër, and P. Scardi, J. Appl. Crystallogr. **33**, 964 (2000).
[28] T. Ungár, J. Gubicza, G. Ribárik, and A. Borbély, J. Appl. Crystallogr. **34**, 298 (2001).
[29] A. Borbély and I. Groma, Appl. Phys. Lett. **79**, 1772 (2001).
[30] D. N. Talwar, M. Vandevyver, K. Kunc, and M. Zigone, Mater. Res. **4**, 71 (2001).
[31] I. C. Dragomir and T. Ungár, J. Appl. Crystallogr. **35**, 556 (2002).
[32] A. L. Patterson, Phys. Rev. **56**, 972 (1939).
[33] P. P. Ewald, Proc. Phys. Soc. London **52**, 167 (1940).
[34] R. Hosemann and S. N. Bagchi, *Direct Analysis of Diffraction by Matter* (North-Holland, Amsterdam, 1962), pp. 260-264.
[35] We remark here that constructions (b) and (c) are less dramatically different than what appears in Ref. 17, depending on a proper choice of the unit cell. A physically descriptive choice, like the Wigner-Seitz unit cell, for instance, would reduce those differences.
[36] For the sake of brevity we omit the factors v_c^{-1} from the Fourier amplitudes and v_c^{-2} from the related intensities, where v_c is the unit cell volume.
[37] Here for simplicity we incorporate the Debye-Waller factor into the form factor: $f_\alpha(q)=f_\alpha^0(q)T_\alpha(q)$, where $f_\alpha^0(q)$ is the (static) atomic form factor of the α-th atom and $T_\alpha(q)=e^{-B_\alpha q^2/4}=e^{-2\pi^2\langle u_\alpha^2\rangle q^2}$ is the relevant Debye-Waller factor; B_α is the crystallographic thermal factor and $\langle u_\alpha^2\rangle$ is the mean-square thermal displacement of the αth atom. Strictly speaking the latter may be a second-rank tensor instead of a scalar, so that T_α depends on $\boldsymbol{q}$ instead of simply q. This is possible only for atoms with noncubic site symmetry. This does not apply to substances considered in this work. However, for completeness, we refer to K. Miura, T. Ino, and N. Minami, Acta Crystallogr., Sect. A: Found. Crystallogr. **43**, 49 (1987) that presents a detailed treatment of the general case.
[38] L. F. Kiss, J. Söderlund, G. A. Niklasson, and C. G. Granqvist, Nanotechnology **10**, 25 (1999).
[39] D. Balzar *et al.*, J. Appl. Crystallogr. **37**, 911 (2004).
[40] http://www.boulder.nist.gov/div853/balzar; http://www.du.edu/~balzar/s-s_rr.htm
[41] A. Cervellino, C. Giannini, A. Guagliardi, and M. Ladisa, J. Appl. Crystallogr. (unpublished).
[42] N. C. Popa, J. Appl. Crystallogr. **33**, 103 (2000).
[43] A. K. Singh and C. Balasingh, J. Appl. Phys. **90**, 2296 (2001).
[44] F. Zhang, S. Chan, J. E. Spanier, E. Apak, Q. Jin, R. D. Robinson, and I. P. Herman, Appl. Phys. Lett. **80**, 127 (2002).
[45] J. A. Nelder and R. Mead, Comput. J. **7**, 308 (1965).
[46] C. Giacovazzo, H. L. Monaco, D. Viterbo, F. Scordari, G. Gilli, G. Zanotti, and M. Catti, *Fundamentals of Crystallography* (IUCr-Oxford University Press; Oxford, 1992), Chap. 5, pp. 321-324.